Autogenous nanofluidic flow facilitates pervasive metamorphism in the Earth's crust

Oliver Plümper[1,*], Alexandru Botan[2], Catherina Los[3], Yang Liu[1,4], Anders Malthe-Sørenssen[2], Bjørn Jamtveit[2]

[1]Department of Earth Sciences, Utrecht University, Budapestlaan 4, 3584CD Utrecht, The Netherlands

[2]Physics of Geological Processes (PGP), University of Oslo, Blindern, N-0136 Oslo, Norway

[3]Department of Geosciences, University of Bremen, Klagenfurter Strasse, 28359 Bremen, Germany

[4]Debye Institute for Nanomaterials Science, Utrecht University, the Netherlands

*corresponding author: o.plumper@uu.nl

The permeability of the Earth's crust controls the redistribution of elements to form ore and hydrocarbon deposits, the release[1] and sequestration[2] of greenhouse gases, and facilitates crustal metamorphism influencing plate rheology[3]. Although fluid flow is often restricted to fractures and shear zones, fluids can pervasively penetrate large volumes of nominally impermeable rocks[4, 5]. Fluid pressure gradients accompanied by deformation are thought to be the main driving forces for permeability creation and fluid flow[4, 6]. Without deformation-induced fluid pathways crustal permeability restricts transport to molecular diffusion mainly along grain boundaries[7, 8]. But there is considerable evidence that metamorphic phase transformations can self-generate fluid pathways[9-12]. It is at the scale of these confined pathways (10s to 100s nm) that fluid transport phenomena may occur that are impossible at larger length scales[13, 14]. Using multi-dimensional nano-imaging and molecular dynamics simulations we show that in feldspar, the most abundant mineral in the Earth's crust, electrokinetic transport phenomena through reaction-induced nanopores (10-100 nm) competes strongly with pressure-driven flow. We suggest

that metamorphic fluid flow is considerably influenced by nanofluidic transport phenomena with profound and unexplored implications for mass transport through the solid Earth.

Understanding the forces driving fluid pathway generation and fluid transmission through these pathways is central to interpreting the amounts and spatiotemporal scales of fluid flow and mass transfer through the solid Earth as well as their feedback on crustal metamorphism and geochemical cycles[5, 15]. The intrinsic rock permeability within most of the lithosphere is, however, too low ($<10^{-17}$ m^2)[6] to transmit sufficient amounts of fluids to explain large-scale fluid-induced metamorphism. Thus, deformational processes such as grain-scale dilatancy, micro-cracking and hydraulic fracturing are typically invoked to explain the generation of interconnected fluid pathways allowing metamorphism to progress[4]. Fluid flow through these pathways is commonly assumed to occur as a response to gradients in fluid pressure and hydraulic head[15], largely described by Navier-Stokes equations. In the absence of macro-scale fluid pathways fluid transport at the scale of grain interfaces (< 1 nm) is traditionally assumed to occur via Fickian diffusion[8] and fluid connectivity is controlled by equilibrium surface energies[7]. However, there is wide evidence that networks of fluid pathways (pores and fractures) in nominally impermeable rocks can emerge solely from coupled reaction-transport processes[1, 5, 9, 10, 16]. These patterns likely reflect the reaction dynamics rather than minimization of surface energies. Complex pore networks, ending at the reaction front, develop in which the majority of pore space is confined to the nanoscale (1 to 100s nm)[9, 17-19]. At this scale, novel transport properties can arise from the combination of strong confinement and the electronic properties of the solid/mineral surface[13, 14]. As the surface-to-volume ratio is substantially increased surface-charge-governed transport phenomena that are impossible in bulk fluids at larger length scales dominate the system. Confinement of water in pore channels of less than two nm in diameter creates huge permeability amplifications, three orders of

magnitude higher than predicted by continuum hydrodynamics[20]. Moreover, osmotically induced electric currents generated by salinity gradients through 40-nm pore channels have been measured that exceed their pressure-driven counterpart by orders of magnitude[21]. Although the emergence of new transport properties at the nanoscale have led to game-changing technological discoveries very little is known about the consequences of nanofluidic transport for fluid-driven systems within the solid Earth.

Herein, we investigate the effect of pore structure and fluid transport through feldspar nanopores (<1 μm; for a pore size definition see Supplementary material X) during massive fluid-induced feldspar replacement reactions (albitization and K-feldspathisation) in the Larvik batholith[22] situated in the Oslo rift area, south-east Norway (Fig. 1a). The batholith comprises a suite of igneous plutons emplaced during intracontinental rifting in the early Permian. Unlike conventional monzonite rocks, larvikite contains a single ternary feldspar ($CaAl_2Si_2O_8$ – $NaAlSi_3O_8$ – $NaAlSi_3O_8$) (Fig. 1b-d). Magma crystallization resulted in an ultralow-permeability igneous rock structure characterized by mm- to cm-sized feldspar crystals with a strong blue iridescence (Fig. 1b-d). Chemical alteration of the larvikite is expressed as a prominent colour change from blue to ochre, making it a unique macroscopic reaction tracer. This discolouration proceeds along grain boundaries (Fig. 2C) and can result in the complete shape-preserving replacement (pseudomorphism) of the original feldspar (Fig. 2D). Chemical analysis shows that the altered, ochre, feldspar is an intergrowth of the feldspar endmembers albite ($NaAlSi_3O_8$) and K-feldspar ($KAlSi_3O_8$) (Supplementary material X). We refer to original (blue) and altered feldspar (ochre) herein. Although feldspar replacement initiated along fractures and faults (Supplementary material X), pervasive alteration occurred without deformation (Fig. 1b-d). Regional-scale geological mapping confirms that alteration occurred across an area of at least 60 km² (Fig. 1a). Microstructures of the feldspar replacement (see below and Fig. 2) are consistent with previous experimental[23] and natural[16] investigations,

showing that the replacement reactions are a result of non-equilibrium fluid-rock interaction. The replacement (blue to ochre feldspar) took place via an interface-coupled dissolution-precipitation mechanism in which the supply of fluid is essential for the reaction to progress[9]. Fluids required to drive the alteration were likely sourced from the intracontinental rift region.

Microstructural analyses of partially altered feldspar grains show that the original and altered feldspar domains are divided by chemically and structurally sharp reaction interfaces (Fig. 2 a-d). Nanopores (<1 μm) exclusively developed within the altered feldspar (Fig. 2 e-g). Nanocrystalline (hydroxy)-Fe-oxide precipitated within some of these pores resulting in the observed discolouration[16] (Supplementary material X). In three-dimensions (Fig. 3) the pore network is defined by spatially aligned pore channels (average diameter: 100 nm) directed towards and ending at the reaction interface. Pore diameters follow a log-normal distribution (Fig. 3b) consistent with a nucleation and growth control on their formation during feldspar replacement. In its present form individual pore channels (y-axis in Figure 3) are transformed into disconnected cavities with high aspect ratios. Disconnection is likely due to a Rayleigh-type instability sponsored by surface energy minimization[24]. The dynamic and transient nature of the pore network during fluid-mediated replacement reactions have previously been highlighted using an ionic salt (KBr-KCl) analogue system[12]. Also in this case interface-orientated, dead-end pore channels develop (see X-ray tomography image in Supplementary Material X), facilitating reaction progress through the continuous supply of fluid to the reaction front[9].

To estimate the transport properties of the confined fluid in a feldspar nanopore we used non-equilibrium molecular dynamics (NEMD) to simulate fluid and mass transport as result of a pressure gradient ∇P, chemical potential gradient of the solute $\nabla \mu$ and electric field gradient $-\nabla E$ parallel to the electrically charged feldspar nanopore wall (Fig. 4A-D). Details regarding the model and simulations can be found in the Methods section. Whereas electro-

osmotic fluid (solvent) flow and mass (solute) transport through nanopores is a well-studied phenomenon[13, 14], flow through chemical potential gradients is commonly associated to osmosis through a semipermeable membrane. Here only the solvent can move from low to high salt concentration. However, in a fully permeable nanopore with charged surface walls fluid movement can occur as a result of $\nabla\mu$ that is reverse to the 'usual' osmotic flow direction, i.e. fluid moves from high to low concentration. The origin in diffusio-osmotic flow lies in the electrostatic attraction of solute molecules to the pore wall, which causes a locally high solute concentration, which in turn generates an osmotic pressure gradient at the pore wall in the same direction as the solute concentration gradient (Supplementary material X). This osmotic pressure gradient generates fluid flow and mass transport. Theoretically predicted and experimental observed fluid flow velocities generated by diffusio-osmosis V_{DO} through idealized nanopores[21] is on the order of several μm s^{-1}. In addition, if liquid slip can occur diffusion-osmotic fluid fluxes might be increased considerably[25]. For simplicity we do not consider atomic-scale surface roughness and feldspar reactivity. Pore walls were modelled as orthoclase feldspar (Methods) allowing us to compare to previous MD simulations[26] and synchrotron X-ray reflectivity experiments[27] that characterized the orthoclase-water interface. Figure 4 B shows the velocity profiles, obtained by NEMD, through a 30 nm feldspar slit pore generated by gradients in ∇P, $\nabla\mu$, $-\nabla E$, respectively. Both, hydrodynamic and diffusio-osmotic velocity profiles are very similar. Electro-osmotic velocities show a separation of ion species (K^+, Cl^-) and strong velocity changes very close (<5 nm) to the charged feldspar surface. Our NEMD results are in agreement with recent analytical predictions[28] of transfer coefficients that couple solvent and ionic fluxes through a charged pore under the effect of ∇P, $\nabla\mu$, $-\nabla E$ (Supplementary material X). On the basis of the Onsager symmetry relations (Supplementary material X), stating that all transport mechanisms are tightly coupled, we can define the overall

volumetric flux J_{vol} [m^3s^{-1}] through a pore channel as a combination of the individual hydrodynamic J_{vol}^{P}, diffusion-osmotic J_{vol}^{C}, and electro-osmotic fluxes J_{vol}^{V} as follows

$$J_{vol} = -K^{P}\nabla P - K^{C}k_{B}T\nabla\mu - K^{V}\nabla E . \quad (1)$$

Here k_B is the Boltzmann constant, T temperature and K^P are the hydrodynamic [m^4 Pa^{-1} s^{-1}], K^C the diffusio-osmotic [m Pa^{-1} s^{-1}], and K^V the electro-osmotic [m^4 V^{-1} s^{-1}] transport coefficients (Supplementary material X). Figure 4 C shows J_{vol} through a 100 nm feldspar pore channel with a length of 1 µm as a function of its individual contributions from gradients in ∇P, $\nabla\mu$, $-\nabla E$. In order to achieve a J_{vol} of 1.5x10^{-15} $m^{-3}s^{-1}$ a pressure drop of 1 bar or a concentration difference (C_2/C_1) between the pore ends of 15% is required. This strong influence of diffusio-osmotic flow to J_{vol} is found across the entire range of pore channel diameters from 5 to 100 nm (Fig. 4D). At pore diameters <25 nm diffusio-osmosis and electro-kinetic fluxes become dominant. Although the analytical predictions presented are in good agreement with our NEMD, the flux predictions are limited to pore diameters of up to ~100 nm, due to the Debye-Hückel linearization of the Poisson-Boltzmann (PB) equation[28].

The NEMD simulations above show that diffusio-osmosis can have a considerable effect on fluid fluxes through feldspar nanopores and that neglecting electrokinetic flow can result in large errors on the overall flow. A simple calculation, based on our MD simulations, shows that a 0.1 M KCl fluid within a 10x10x100 nm pore contains 535 K atoms. Thus only 80 atoms, equivalent to C_2/C_1 = 15%, must be released or consumed during the dissolution-precipitation-mediated replacement reaction to induce a diffusio-osmotic flux that is equivalent to a 1 bar pressure difference. Assuming a dissolution rate[29] of 5-50 atoms s^{-1} and pore wall diameter of 100 nm, corresponding to 80,000 surface-exposed K atoms, a concentration gradient to drive diffusion-osmotic flow can be established nearly instantaneously during feldspar replacement. Equally important as the generation of concentration gradients is the

maintenance of surface charge at pore walls. Although we used a charged (010) orthoclase surface that has a dipole moment in the direction normal to its surface[26] and will thus undergone surface reconstruction over time, dynamic dissolution-precipitation will transiently expose surfaces with elevated energies facilitating diffusio-osmotic flow. Indeed, recent experiments shown first indications that convective motion in dead-end pore channels during (pseudomorphic) mineral replacement reactions occurs as a result of self-induced diffusio-osmotic flow[30]. To advance our understanding of these novel transport processes future studies need to couple the hydrodynamic and electrokinetic transport with kinetics and crystallographic evolution of the rock pore network.

In conclusion, we propose that in non-equilibrium reactive systems such as the one presented here, where fluid pathways emerge and evolve dynamically as a result of dissolution and precipitation, fluid flow through reaction-induced pores and fractures, particularly at the nanoscale, can be self-generated through the emergence of transient concentration gradients and surface charges. Fluid and mass transport through diffusio-osmosis is substantially faster than classical diffusion, and thus may have a profound effect on metamorphic reaction rates. Autogenous nanofluidic flow may considerably aid large-scale metamorphic fluid flow independent of tectonic deformation and massive fluid pressure gradients.

References

1. Ague, J. J. & Nicolescu, S. Carbon dioxide released from subduction zones by fluid-mediated reactions. *Nature Geoscience* **7**, 355-360 (2014).

2. Matter, J. M. *et al*. Rapid carbon mineralization for permanent disposal of anthropogenic carbon dioxide emissions. *Science* **352**, 1312-1314 (2016).

3. Jackson, J., Austrheim, H., McKenzie, D. & Priestley, K. Metastability, mechanical strength, and the support of mountain belts. *Geology* **32**, 625-628 (2004).

4. Oliver, N. Review and classification of structural controls on fluid flow during regional metamorphism. *J. Metamorph. Geol.* **14**, 477-492 (1996).

5. Jamtveit, B., Austrheim, H. & Putnis, A. Disequilibrium metamorphism of stressed lithosphere. *Earth-Sci. Rev.* **154**, 1-13 (2016).

6. Manning, C. & Ingebritsen, S. Permeability of the continental crust: Implications of geothermal data and metamorphic systems. *Rev. Geophys.* **37**, 127-150 (1999).

7. Watson, E. B. & Brenan, J. M. Fluids in the lithosphere, 1. Experimentally-determined wetting characteristics of CO2H2O fluids and their implications for fluid transport, host-rock physical properties, and fluid inclusion formation. *Earth Planet. Sci. Lett.* **85**, 497-515 (1987).

8. Dohmen, R. & Milke, R. Diffusion in polycrystalline materials: grain boundaries, mathematical models, and experimental data. *Reviews in Mineralogy and Geochemistry* **72**, 921-970 (2010).

9. Putnis, A. Mineral replacement reactions. *Reviews in mineralogy and geochemistry* **70**, 87-124 (2009).

10. Kelemen, P. B. & Hirth, G. Reaction-driven cracking during retrograde metamorphism: Olivine hydration and carbonation. *Earth Planet. Sci. Lett.* **345**, 81-89 (2012).

11. Plümper, O., Røyne, A., Magrasó, A. & Jamtveit, B. The interface-scale mechanism of reaction-induced fracturing during serpentinization. *Geology* **40**, 1103-1106 (2012).

12. Raufaste, C., Jamtveit, B., John, T., Meakin, P. & Dysthe, D. K. *The mechanism of porosity formation during solvent-mediated phase transformations* (Proceedings of the Royal Society of London A: Mathematical, Physical and Engineering Sciences Ser. 467, The Royal Society, 2011).

13. Schoch, R. B., Han, J. & Renaud, P. Transport phenomena in nanofluidics. *Reviews of modern physics* **80**, 839 (2008).

14. Bocquet, L. & Charlaix, E. Nanofluidics, from bulk to interfaces. *Chem. Soc. Rev.* **39**, 1073-1095 (2010).

15. Ague, J. Fluid flow in the deep crust. *Treatise on geochemistry* **3**, 659 (2003).

16. Plümper, O. & Putnis, A. The complex hydrothermal history of granitic rocks: multiple feldspar replacement reactions under subsolidus conditions. *J. Petrol.*, egp028 (2009).

17. Tutolo, B. M., Mildner, D. F., Gagnon, C. V., Saar, M. O. & Seyfried, W. E. Nanoscale constraints on porosity generation and fluid flow during serpentinization. *Geology* **44**, 103-106 (2016).

18. Navarre-Sitchler, A. K. *et al*. Porosity and surface area evolution during weathering of two igneous rocks. *Geochim. Cosmochim. Acta* **109**, 400-413 (2013).

19. Milke, R., Neusser, G., Kolzer, K. & Wunder, B. Very little water is necessary to make a dry solid silicate system wet. *Geology* **41**, 247-250 (2013).

20. Holt, J. K. *et al*. Fast mass transport through sub-2-nanometer carbon nanotubes. *Science* **312**, 1034-1037 (2006).

21. Siria, A. *et al*. Giant osmotic energy conversion measured in a single transmembrane boron nitride nanotube. *Nature* **494**, 455-458 (2013).

22. Else-Ragnhild, N. Petrogenesis of the Oslo Region larvikites and associated rocks. *J. Petrol.* **21**, 499-531 (1980).

23. Hövelmann, J., Putnis, A., Geisler, T., Schmidt, B. C. & Golla-Schindler, U. The replacement of plagioclase feldspars by albite: observations from hydrothermal experiments. *Contributions to Mineralogy and Petrology* **159**, 43-59 (2010).

24. Colin, J., Grilhé, J. & Junqua, N. Morphological instabilities of a stressed pore channel. *Acta materialia* **45**, 3835-3841 (1997).

25. Ajdari, A. & Bocquet, L. Giant amplification of interfacially driven transport by hydrodynamic slip: Diffusio-osmosis and beyond. *Phys. Rev. Lett.* **96**, 186102 (2006).

26. Kerisit, S., Liu, C. & Ilton, E. S. Molecular dynamics simulations of the orthoclase (001)- and (010)-water interfaces. *Geochim. Cosmochim. Acta* **72**, 1481-1497 (2008).

27. Fenter, P., Cheng, L., Park, C., Zhang, Z. & Sturchio, N. Structure of the orthoclase (001)- and (010)-water interfaces by high-resolution X-ray reflectivity. *Geochim. Cosmochim. Acta* **67**, 4267-4275 (2003).

28. Obliger, A. *et al*. Numerical homogenization of electrokinetic equations in porous media using lattice-Boltzmann simulations. *Physical Review E* **88**, 013019 (2013).

29. Fenter, P. *et al*. Orthoclase dissolution kinetics probed by in situ X-ray reflectivity: effects of temperature, pH, and crystal orientation. *Geochim. Cosmochim. Acta* **67**, 197-211 (2003).

30. Kar, A. *et al*. Self-Generated Electrokinetic Fluid Flows during Pseudomorphic Mineral Replacement Reactions. *Langmuir* (2016).

31. Colville, A. & Ribbe, P. Crystal structure of an adularia and a refinement of structure of orthoclase. *Am. Mineral.* **53**, 25-& (1968).

32. Plimpton, S. Fast parallel algorithms for short-range molecular dynamics. *Journal of computational physics* **117**, 1-19 (1995).

33. Yoshida, H., Mizuno, H., Kinjo, T., Washizu, H. & Barrat, J. Molecular dynamics simulation of electrokinetic flow of an aqueous electrolyte solution in nanochannels. *J. Chem. Phys.* **140**, 214701 (2014).

Acknowledgements

The paper greatly benefited from discussions with H.E. King, H. Austrheim. B.J. and O.P thank R. Sørensen for providing the geological map and S. Dahlgren for field work assistance. O.P. and K.L. thank A. Barnhoorn for assistance with X-ray tomography. O.P. was supported

through a Veni grant (863.13.006), awarded by the Netherlands Organisation for Scientific Research (NWO).

Author contributions

O.P. designed the research; O.P. and B.J. did the field work; O.P., C.L. and Y.L. collected and interpreted the microstructural and chemical data; all authors participated in data interpretation of the; O.P., A.B., B.J. and A.M.S. developed the model.

Additional information

Supplementary information is available in the online version of the paper. Reprints and permissions information is available at www.nature.com/reprints. Correspondence and requests for materials should be addressed to O.P. (o.plumper@uu.nl).

Competing financial interests

The authors declare no competing financial interests.

Methods

Focused ion beam scanning electron microscopy/transmission electron microscopy (FIB-SEM/TEM). Electron-transparent thin foils were prepared for (scanning) transmission electron microscopy ((S)TEM) by using a FEI Helios Nanolab G3 focused ion beam - scanning electron microscope (FIB-SEM). The FIB-SEM was also used to acquire several slice-and-view series for 3D volume reconstructions. Slice imaging was carried out in backscattered electron mode at 2 kV and 1.6 nA with a voxel size of 8×8×30 nm^3. All FIB-SEM nanotomography volumes were reconstructed and analysed using FEI Avizo Fire 9. Thin foils were investigated in a FEI Talos F200X (S)TEM equipped with four energy-dispersive X-ray detectors (Super-EDX). All FIB-SEM and TEM analyses were carried out at the Microscopy Square, Utrecht University.

Feldspar surface generation. We considered a slab of orthoclase ($KAlSi_3O_8$) with the following experimental unit cell parameters[31]: a=8.554 Å, b=12.97 Å, c=7.207 Å, α=90º, β=116.01º, γ=90º. A (010) orthoclase slab was generated and cut along the cleavage plane β

(for more details see Kerisit et al.[26]). Hydrogen atoms were added to form hydroxyl groups on both slab surfaces. The surface charge of -0.25 e/nm^2 was achieved through tetrahedral substitution of Si by Al. This corresponds to a pH of x (CITE), typical for crustal fluids (Yardley). The slab consisted of 9×9 unit cells with a thickness of approximately 25 Å was divided in two parts located at the top and bottom of the simulation box and forms a section of slit-like pore, as shown in Figure 1A. The pore space is filled by water, K^+ and Cl^- corresponding to a 0.1 M solution at 500K and 200 bar. All parameters describing the interactions between particles can be found in Kerisit, 2008. The positions of all orthoclase atoms were fixed.

Molecular dynamics simulations. Molecular dynamics (MD) simulations (including non-equilibrium dynamics) were carried out with the open-source LAMMPS[32] simulation package in a canonical ensemble. A constant temperature of 500 K was maintained with a Nosé-Hoover thermostat. The equations of motion were integrated using a 1 fs time step and the SHAKE algorithm. To investigate the transport properties of the confined fluid we simulated, using non-equilibrium MD, a pressure gradient, chemical potential gradient of the solute and electric field parallel to the surface by applying constant external forces to the fluid atoms[33]. Simulations were performed for pore widths of 30, 50 and 100 nm, respectively. For pressure-driven flow we used forces of 1.25×10^{-5}, 7.5×10^{-6} and 4×10^{-7} kcal/mol/A. The chemical potential gradient of the solute was achieved by applying 0.01, 0.03 and 3×10^{-4} kcal/mol/A to the ions. Electro-osmotic flow was simulated by applying an electric field of 0.03 V/A to all pores. The velocities of the particles are collected every ps for 10 ns, after an equilibration period of 25 ns. The volume flow rates for cylindrical pores were obtained by integrating the flux profiles J_{cyl} of the slit pores by $J_{cycl} = \pi \int_{-\frac{L}{2}}^{\frac{L}{2}} J_{slit}^2(z)dz$, where L is the pore length and z the pore diameter.

Figures and captions

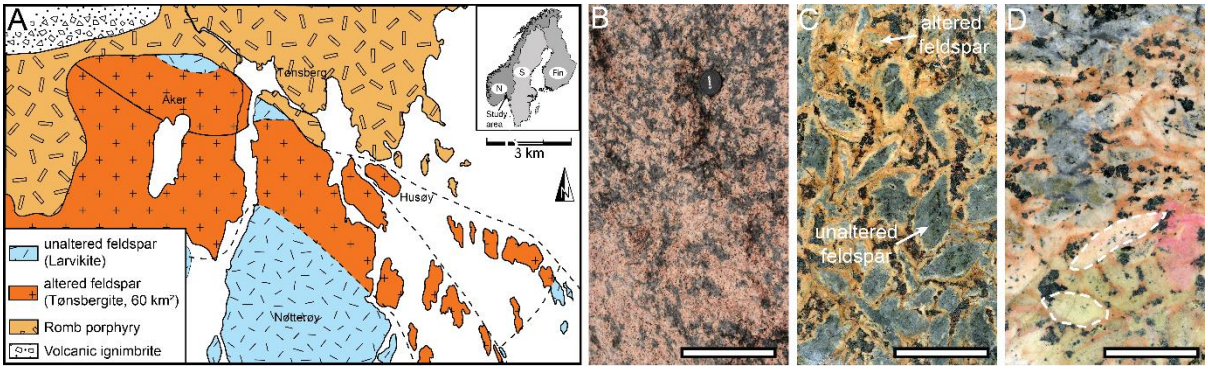

Figure 1 Massive fluid-induced feldspar alteration in the Larvikite batholith, Norway. (A) Geological map showing the extent of feldspar alteration across 60 km². Inset shows the geographic location of the study area. (B) Partly altered larvikite. Unaltered feldspars are dark blue, whereas the altered feldspar appears ochre-colored. (C) –(D) Magnified views showing the partial feldspar replacement. A replacement goes to completion the original shape remains (pseudomorphism; dashed areas in (D).

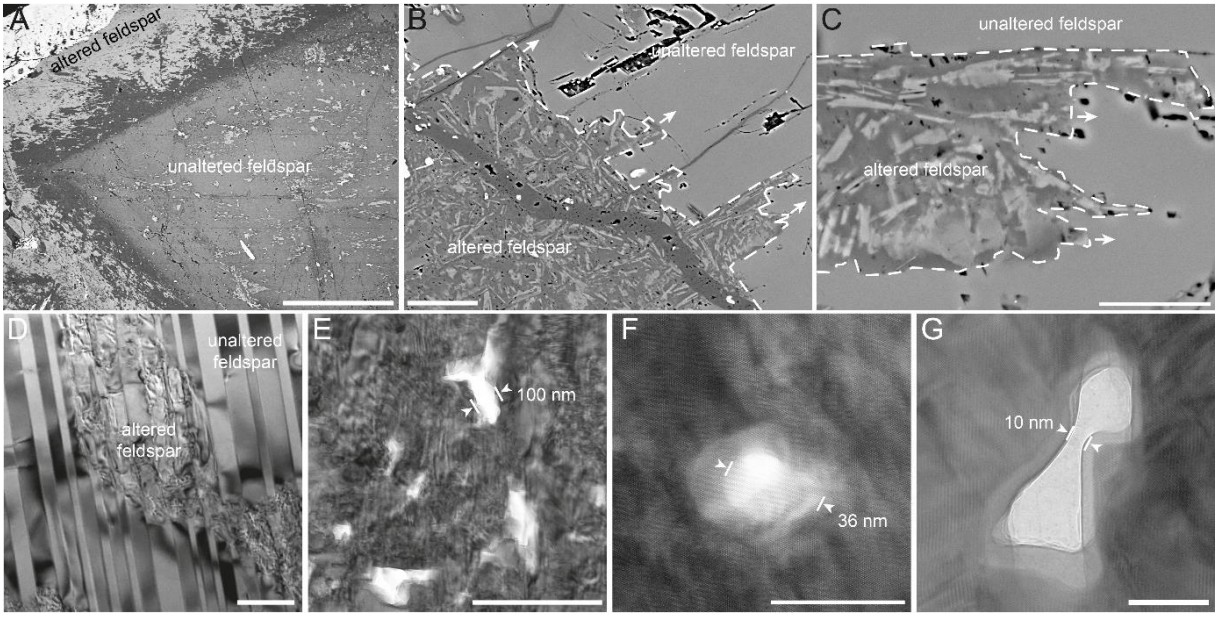

Figure 2 Micro- and nano-structures of feldspar alterations and mineral replacement interfaces. (A) Backscattered electron image giving an overview of a partly replaced feldspar. (B)-(C) Show sharp reaction fronts dividing pore-free, original feldspar and pore-bearing, altered feldspar. The direction of replacement is given by arrows. (D) Bright-field transmission electron microscopy (BF-TEM) image showing the replacement interface and the crystallographic continuity of the original feldspar twinning. (E) Pore distribution in original feldspar. (F) and (G) high resolution (HR-) TEM images of two nanopores.

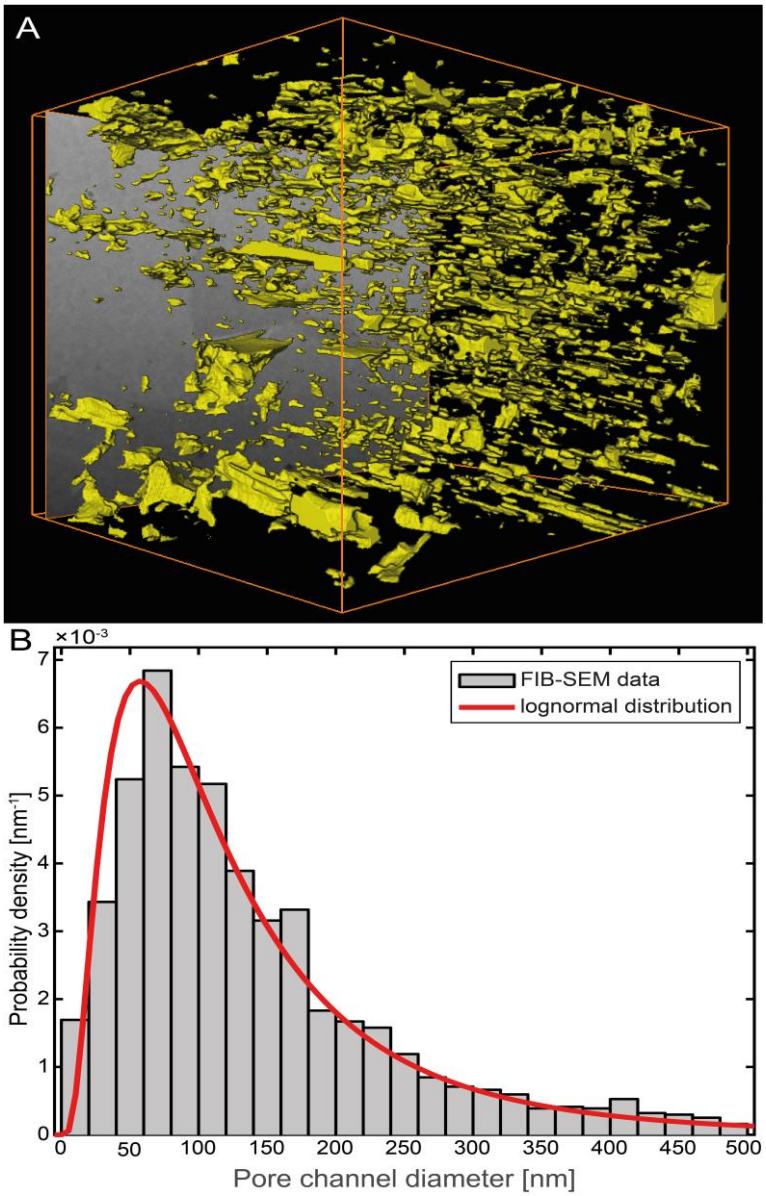

Figure 3 Nanopore feldspar channel network in altered feldspar. (A) Three-dimensional visualization of pore network using focused-ion-beam-assisted nanotomography. (B) Probability density of pore channel diameter. The distribution is lognormal and has median diameter of 100 nm.

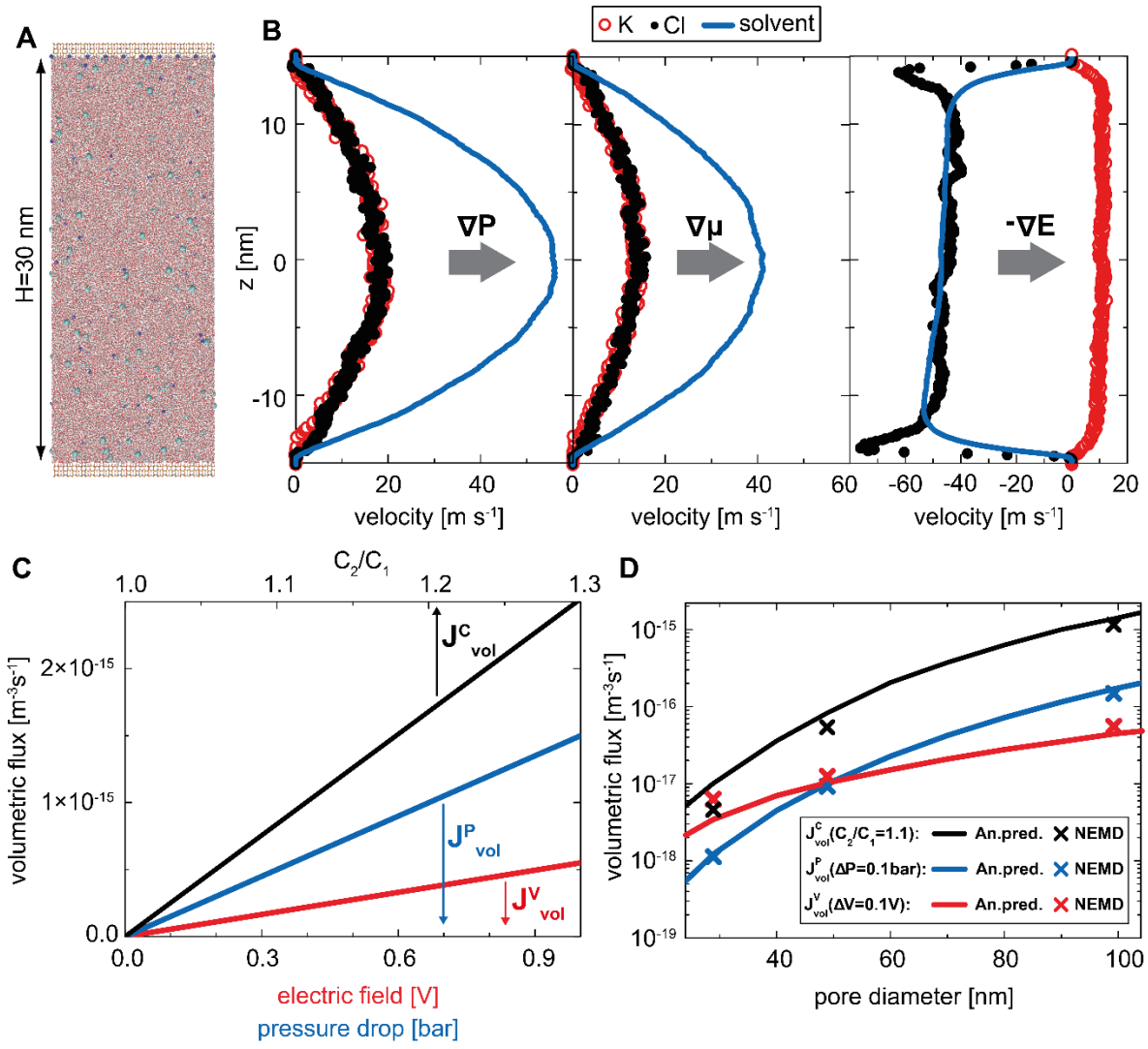

Figure 4 Molecular dynamics simulations of hydrodynamic and electrokinetic fluid flow through a feldspar nanopore. (A) Snapshot of the simulation box with 3D periodic boundary conditions: green, X; blue: Na; red, O; white, H. (B) Velocity profiles of solvent (H_2O), K^+ and Cl^- sponsored by a pressure-gradient ∇P (hydrodynamic flow), solute-gradient $\nabla \mu$ (diffusio-osmosis) and electric field-gradient $-\nabla E$. Velocity profiles for the pressure- and solute-gradient are almost identical. (C) Comparison of volumetric fluxes achievable through electric field J_{vol}^{V}, pressure drop J_{vol}^{P} and chemical gradient J_{vol}^{C} through a cylindrical feldspar pore (diameter 100 nm; length 1 µm). (D) Volumetric flux as a function of pore diameter with given boundary conditions of $J_{vol}^{V}, J_{vol}^{P}, J_{vol}^{C}$. Analytical predictions (An. pred.) are in agreement with NEMD simulations.